



# Insight into the crystal structures and physical properties of the uranium borides

**UB<sub>1.78±0.02</sub>, UB<sub>3.61±0.041</sub> and UB<sub>11.19±0.13</sub>**

Laura Martel, Thibault Charpentier, Pedro Amador Cedran, Chris Selfslag, Mohamed Naji, Jean-Christophe Griveau, Eric Colineau, Rachel Eloirdi

## ► To cite this version:

Laura Martel, Thibault Charpentier, Pedro Amador Cedran, Chris Selfslag, Mohamed Naji, et al.. Insight into the crystal structures and physical properties of the uranium borides UB<sub>1.78±0.02</sub>, UB<sub>3.61±0.041</sub> and UB<sub>11.19±0.13</sub>. *Minerals*, 2022, 12(1), pp.29.10.3390/min12010029.cea-03507034

HAL Id: cea-03507034

<https://cea.hal.science/cea-03507034>

Submitted on 3 Jan 2022

**HAL** is a multi-disciplinary open access archive for the deposit and dissemination of scientific research documents, whether they are published or not. The documents may come from teaching and research institutions in France or abroad, or from public or private research centers.

L'archive ouverte pluridisciplinaire **HAL**, est destinée au dépôt et à la diffusion de documents scientifiques de niveau recherche, publiés ou non, émanant des établissements d'enseignement et de recherche français ou étrangers, des laboratoires publics ou privés.



Distributed under a Creative Commons Attribution 4.0 International License

Article

# Insight into the Crystal Structures and Physical Properties of the Uranium Borides $\text{UB}_{1.78 \pm 0.02}$ , $\text{UB}_{3.61 \pm 0.041}$ and $\text{UB}_{11.19 \pm 0.13}$

Laura Martel <sup>1,\*</sup>, Thibault Charpentier <sup>2</sup>, Pedro Amador Cedran <sup>1</sup>, Chris Selfslag <sup>1</sup>, Mohamed Naji <sup>3</sup>, Jean-Christophe Griveau <sup>1</sup>, Eric Colineau <sup>1</sup> and Rachel Eloirdi <sup>1</sup>

<sup>1</sup> European Commission, Joint Research Centre (JRC), 76125 Karlsruhe, Germany; Pedro.AMADOR-CELDTRAN@ec.europa.eu (P.A.C.); Chris.SELFSLAG@ec.europa.eu (C.S.); Jean-Christophe.GRIVEAU@ec.europa.eu (J.-C.G.); Eric.COLINEAU@ec.europa.eu (E.C.); Rachel.ELOIRDI@ec.europa.eu (R.E.)

<sup>2</sup> CEA, CNRS, NIMBE, Université Paris-Saclay, CEDEX, 91191 Gif-sur-Yvette, France; thibault.charpentier@cea.fr

<sup>3</sup> LPAIS, University of Sidi Mohamed Ben Abdellah, Fez 30000, Morocco; mnaji.mail@gmail.com

\* Correspondence: lpm.martel@gmail.com

**Abstract:** In this study we reported the synthesis of three polycrystalline uranium borides  $\text{UB}_{1.78 \pm 0.02}$ ,  $\text{UB}_{3.61 \pm 0.041}$ , and  $\text{UB}_{11.19 \pm 0.13}$  and their analyses using chemical analysis, X-ray diffraction, SQUID magnetometry, solid-state NMR, and Fourier transformed infrared spectroscopy. We discuss the effects of stoichiometry deviations on the lattice parameters and magnetic properties. We also provide their static and MAS-NMR spectra showing the effects of the 5f-electrons on the  $^{11}\text{B}$  shifts. Finally, the FTIR measurements showed the presence of a local disorder.



**Citation:** Martel, L.; Charpentier, T.; Amador Cedran, P.; Selfslag, C.; Naji, M.; Griveau, J.-C.; Colineau, E.; Eloirdi, R. Insight into the Crystal Structures and Physical Properties of the Uranium Borides  $\text{UB}_{1.78 \pm 0.02}$ ,  $\text{UB}_{3.61 \pm 0.041}$  and  $\text{UB}_{11.19 \pm 0.13}$ . *Minerals* **2022**, *12*, 29. <https://doi.org/10.3390/min12010029>

Academic Editors: Luis Sánchez-Muñoz and Pierre Florian

Received: 30 November 2021

Accepted: 20 December 2021

Published: 24 December 2021

**Publisher's Note:** MDPI stays neutral with regard to jurisdictional claims in published maps and institutional affiliations.



**Copyright:** © 2021 by the authors. Licensee MDPI, Basel, Switzerland. This article is an open access article distributed under the terms and conditions of the Creative Commons Attribution (CC BY) license (<https://creativecommons.org/licenses/by/4.0/>).

## 1. Introduction

Borides have been studied for their properties such as hardness, stability to radiolytic decay, chemical inertness, and magnetism. Three main applications made them of particular interest: (i) their consideration as an alternative intermediate storage form for actinide elements due to their high refractory properties [1], (ii) their potential formation in sodium cooled fast reactors because of a core melt during reaction of the  $\text{B}_4\text{C}$  control rods with the  $\text{UO}_2$  fuel [2], and (iii) their possibility as candidate constituents for multi-phase accident tolerant fuel [3]. In the uranium-boron phase diagram, three compounds have been reported to exist:  $\text{UB}_2$ ,  $\text{UB}_4$ , and  $\text{UB}_{12}$  [4,5].

They are mostly synthesized by arc-melting elemental uranium and boron in stoichiometric amounts. Nevertheless, due to boron evaporation, non-stoichiometric  $\text{UB}_X$  ( $X = 2 \pm x$ ,  $4 \pm x$ , or  $12 \pm x$ ) phases and additional  $\text{UB}_X$  or  $\text{UO}_2$  phases are often detected. Brewer et al. [6] reported the detection of  $\text{UB}_2$  in samples containing 25 to 75 atomic %B and  $\text{UB}_4$  in samples containing 75 to 85 atomic %B. The magnetic properties of the  $\text{UB}_X$  ( $X = 2, 4, 12$ ) are intensively studied in the literature. Indeed,  $\text{UB}_{2-x}$  is a Pauli paramagnet and a compensated metal with closed Fermi surfaces [7].  $\text{UB}_{4-x}$  is a magnetic compensated metal, but also a moderate heavy fermion where a cross-over is observed between itinerant 5f electrons at low temperatures and localized 5f electrons at high temperature with a Curie–Weiss behavior [8,9]. Finally,  $\text{UB}_{12-x}$  is a Pauli paramagnet and compensated metal, with speculations of superconductivity below 0.4 K [10,11]. Nevertheless, the slight composition/impurities effects on the magnetism has been reported [12] but not thoroughly discussed.

Here, we present the synthesis of  $\text{UB}_{1.78 \pm 0.02}$ ,  $\text{UB}_{3.61 \pm 0.041}$ , and  $\text{UB}_{11.19 \pm 0.13}$  by arc melting, their room temperature crystal structure by XRD and low temperature single crystal XRD (100 K to 300 K), and their magnetic susceptibility and their local structure determined by  $^{11}\text{B}$  nuclear magnetic resonance (NMR) and Fourier transformed infrared

(FTIR) spectroscopy. We discuss our results in comparison with the literature and clarify the differences observed based mostly on composition effects.

## 2. Materials and Methods

The samples were prepared by arc melting of the constituent elements, uranium metal and boron, under a high purity argon atmosphere (6N), on a water-cooled copper hearth. Metallic zirconium in the chamber acts as a getter for oxygen. The UB<sub>x</sub> ingots were melted and turned several times to achieve homogenous samples. To minimise oxidation, the samples were stored under high vacuum ( $\sim 10^{-6}$  mbar). Chemical analyses to determine the B/U ratio were done using Inductively coupled plasma mass spectrometry (ICPMS). The oxygen content was measured via a direct combustion using the infrared absorption detection technique with an ELTRA ONH-2000 instrument. The detection limit for oxygen was determined by measuring a blank 10 times, and the standard deviation of these measurements multiplied by 2.33 was considered as the detection limit. Powder X-ray diffraction analyses were performed on a Bruker Bragg-Brentano D8 advanced diffractometer (Cu K $\alpha$ 1 radiation at a wavelength of 1.5406 Å) equipped with a Ge (111) monochromator and a Lynxeye linear position sensitive detector. The powder patterns were recorded at room temperature using a step size of 0.01973° with an exposure of 4 s across the angular range  $15^\circ \leq 2\theta \leq 120^\circ$ . Operating conditions were 40 kV and 40 mA. The Rietveld refinement was implemented using the program Topas version 4.1. Single crystals of UB<sub>x</sub> selected from the as-cast samples were measured between 100 and 300 K on a Bruker APEX II Quazar diffractometer (Mo-K $\alpha$  radiation, graphite monochromator,  $\lambda = 0.71073$  Å) to follow the lattice parameters versus the temperature. Infrared spectra were recorded on a Bruker Alpha-P FT-IR spectrometer equipped with a “platinum” attenuated total reflection sample module. Using the Origin 2021 software, each main peak was selected. All the samples were analyzed on a 9.4T Bruker NMR spectrometer (<sup>11</sup>B frequency at 128.38 MHz) adapted for the study of nuclear materials. To avoid skin-depth effects and for better RF penetration, powders were used by crushing the bulk samples. A 1.3 mm probe was used and the samples were spun at 40 kHz. A one pulse experiment was performed with a 90° pulse of 1 μs with optimised recycling delays of 0.5 s to 2 s. For UB<sub>11.19</sub> and UB<sub>3.61</sub>, the full static spectra were obtained using the variable offset cumulative spectrum (VOCS) technique [13,14]. The samples were referenced to 1 M H<sub>3</sub>BO<sub>3</sub> (liq.) as an external reference at 19.6 ppm. All the spectra were fitted using the dmfit software [15] and home-built software [16].

## 3. Results and Discussion

### 3.1. Chemical Analyses and X-ray Diffraction

After preparation by arc melting, each sample was analyzed by chemical analyses to define the U/B ratio and eventual oxygen content. Table 1 summarizes the results. Analyses of O content in the sample were successfully done and the quantity was below 200 ppm (detection limit of the instrument). This enabled us to demonstrate the quality of the samples prepared by arc-melting. In the following section, to underline the non-stoichiometry, we call the samples UB<sub>1.78</sub>, UB<sub>3.61</sub>, and UB<sub>11.19</sub>, implying that the composition uncertainty is included. The atomic percentage loss in boron goes from 11, 10 to 7 at% for the samples with formal composition UB<sub>2</sub>, UB<sub>4</sub>, and UB<sub>12</sub>, respectively. The atomic% of boron falls within the composition range of UB<sub>2</sub> and UB<sub>4</sub> described by Brewer et al. [6]. Usually, excess of 5 to 10 wt% in boron is added to reach a pure stoichiometry but, as the different phase structure exists within a range of composition of U/B ratio [6], we did not compensate for the boron loss. We also wanted to avoid the formation of additional phases in the samples.

**Table 1.** U/B ratio obtained by ICPMS and oxygen content determined by direct combustion—irradiated absorption.

Samples	$\text{UB}_{2-x}$	$\text{UB}_{4-x}$	$\text{UB}_{12-x}$
U/B (at/at)	$1.780 \pm 0.020$	$3.613 \pm 0.041$	$11.19 \pm 0.13$
Oxygen content (mg/g)		<200 *	

\* Detection limit of the method.

The XRD patterns reported in Figure 1 and Figure S1 prove well crystallized samples—narrow peaks with high intensities. One crystalline phase was detected for  $\text{UB}_{1.78}$  and  $\text{UB}_{11.19}$ , unlike  $\text{UB}_{3.68}$  where an admixture of 5 wt% of  $\text{UB}_{2-x}$  was detected. The corresponding lattice parameters, crystal structures, and phase compositions are reported in Table 2. In the U–B phase diagram,  $\text{UB}_2$  crystallizes in the hexagonal crystal structure,  $\text{UB}_{12}$  in the cubic crystal structure, and  $\text{UB}_4$  in the tetragonal crystal structure (insets Figure 1).

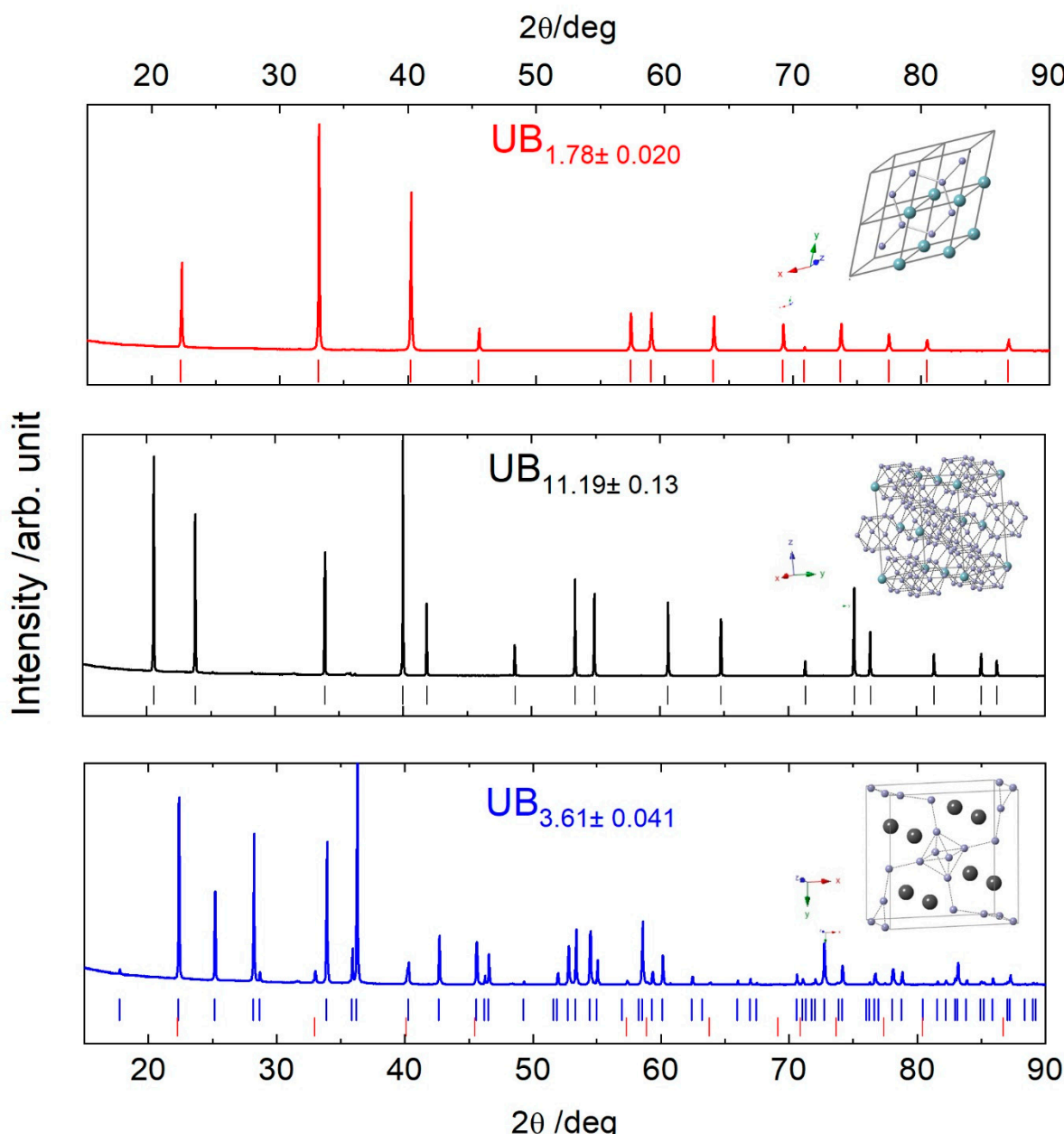


**Figure 1.** X-ray diffraction patterns and structures of the uranium borides. The uranium atoms are bigger than the B atoms.

**Table 2.** Structural parameters.

Name	UB <sub>1.78</sub>	UB <sub>11.19</sub>	UB <sub>3.61</sub>
Structure	hexagonal	cubic	tetragonal
Space group n°	P6/mmm	Fm-3m	P4/mmbm
a = b/Å	3.1225 (1)	7.4715 (1)	7.0777 (4)
c/Å	3.9858 (2)	-	3.9783 (2)
α/deg	90	90	90
β/deg	-	-	-
γ/deg	120	-	-
Rwp	8.38	10.24	9.01
Gof	2.81	3.16	3.05
Composition/%	100	100	95.1 (+UB <sub>2</sub> )
Shortest U-U spacing Å	3.12	5.28	3.65

Despite the numerous studies of UB<sub>2±x</sub>, UB<sub>4-x</sub>, and UB<sub>12-x</sub>, and the known range of non-stoichiometry, only few studies in the open literature link the effects of lattice parameters with composition. According to the previously stated Brewer definition, each UB<sub>X</sub> exists over a range of stoichiometry. Nevertheless, it is clear from the literature that this lower boron content can directly be seen on the lattice parameters. The lattice parameters of the present study and those found in the open literature are given in Table 3. With its lower boron content, UB<sub>1.78</sub>, possesses a lower a lattice parameter compared to UB<sub>1.79</sub> (a = 3.1309 (5) Å, c = 3.9837 (5) Å) [17] and UB<sub>2.02</sub> (a = 3.133 (1) Å, c = 3.9860 (1) Å). Despite the close stoichiometry between our sample and UB<sub>1.79</sub>, the lattice parameters are slightly different, probably due to the impurities indicated by the previous authors (U and UB<sub>4</sub>), which might modify the overall UB<sub>2-x</sub> stoichiometry. For UB<sub>11.78</sub>, the only reported UB<sub>12-x</sub> stoichiometry in the open literature was UB<sub>16</sub> [18] (a = 7.475 Å), which indeed differs from ours. Finally, the UB<sub>3.98</sub> (a = 7.0764 Å, c = 3.9811 Å) sample synthesized by Menovsky et al. [19] is the closest to UB<sub>4</sub> stoichiometry that we could find in the open literature. Compared to our present UB<sub>4-x</sub> sample, the lattice parameters a decrease whereas c slightly increase.

**Table 3.** Lattice parameters of UB<sub>2±x</sub>, UB<sub>4-x</sub>, and UB<sub>12-x</sub> reported in the present study (P.S.) and from the literature.

UB <sub>2</sub>		UB <sub>X</sub>		UB <sub>4</sub>		UB <sub>X</sub>		UB <sub>12</sub>		UB <sub>X</sub>	
a (Å)	c (Å)	Ref.	X	a (Å)	c (Å)	Ref.	X	a (Å)	Ref.	X	
1	3.1225	3.9858	P.S.	1.78 (2)	7.0573	3.9008	[20]	7.468	[21] <sup>1</sup>		
2	3.1302 (3)	3.9878 (3)	[20]		7.0777	3.9783	P.S.	3.613 (41)	7.4715	P.S.	11.19 (13)
3	3.132	3.986	[7] <sup>2</sup>		7.080	3.978	[21]		7.473	[22]	
4	3.139	3.994	[23]		7.079 (1)	3.983 (1)	[24]		7.474	[10] <sup>3</sup> , [11]	
5	3.133	3.986	[25]	2.02	7.0795	3.9794	[26] <sup>4</sup>		7.475	[18,20]	16
6	3.084	4.020	[27]		7.0764	3.9811	[19]	3.98			
7	3.136 (6)	3.988 (8)			7.08	3.98	[9]				
8	3.1309 (5)	3.9837 (5)	[17]	1.79 (6)							

<sup>1</sup> +UB<sub>12</sub> diamagnetic; <sup>2</sup> +impurities; <sup>3</sup> +UB<sub>4</sub>; <sup>4</sup> +amorphous carbon.

In addition to the room temperature XRD, we also performed single crystal measurements at low temperatures. Figure 2 shows the variation of lattice parameters and volume with temperature. For a direct and relative comparison, we used 0.2 Å length scale for all the lattice parameters. At room temperature, we observed a difference between the values recorded on the powders and the four circle. For UB<sub>2-x</sub> a = 3.1444 (62) c = 4.0035 (79); for UB<sub>12-x</sub> a = 7.4789 (15); and for UB<sub>4-x</sub> a = 7.1036 (40), c = 4.009 (42). This difference can be explained by a higher experimental uncertainty of the four-circle at room temperature and to the different sampling used between both measurements. Indeed, the stoichiometry in the powder sample average out all the lattice parameters values. We could fit both lattice

parameters and volumes using linear equations given in Table 4. For  $\text{UB}_{2-x}$  (Figure 2a) and  $\text{UB}_{4-x}$  (Figure 2c), the lattice parameters are decreasing with decreasing temperatures. For  $\text{UB}_{12-x}$  (Figure 2b), the lattice parameters are slightly increasing with decreasing temperatures. We calculated the lattice thermal expansion using the formula in ref. [28] (Figure 2b, bottom) but did not observe a negative minimum such as in  $\text{LuB}_{12}$  or  $\text{YB}_{12}$  [29]. This steep negative thermal expansion might exist at lower temperatures, but such analysis was not possible with our four-circle equipment.

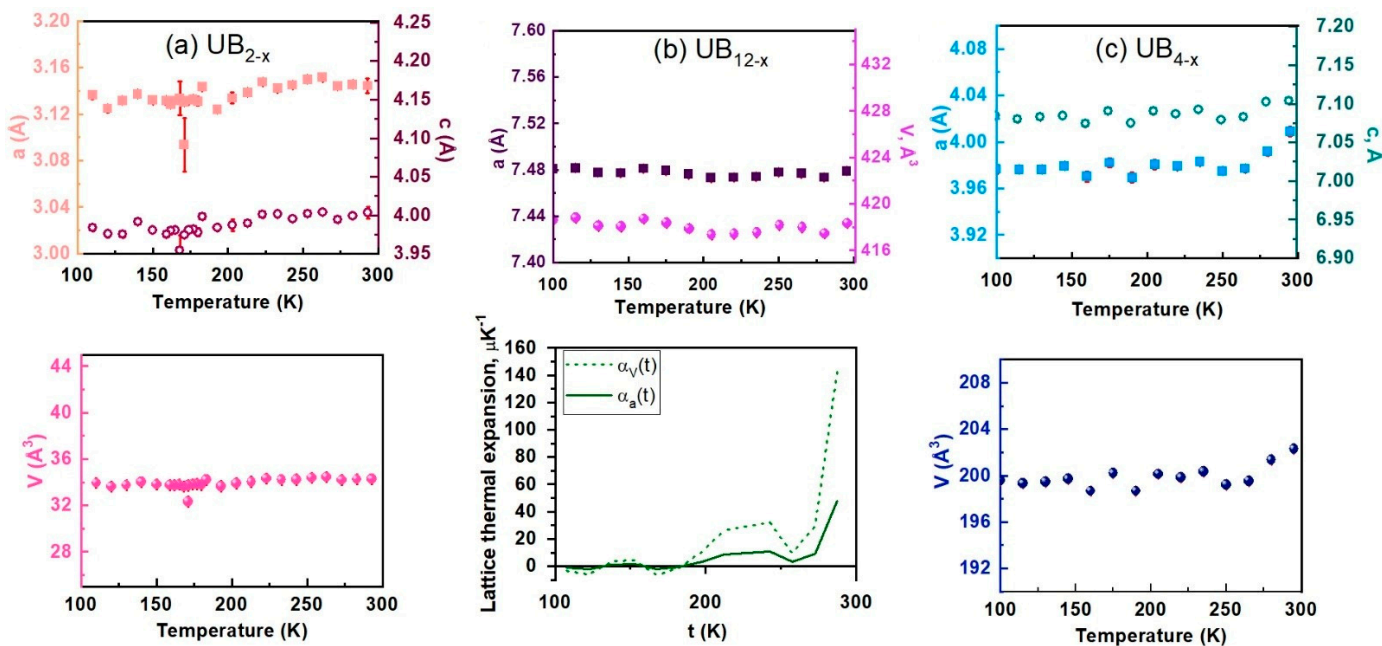


**Figure 2.** Lattice parameters and volume expansion of (a)  $\text{UB}_{2-x}$ , (b)  $\text{UB}_{4-x}$ , and (c)  $\text{UB}_{12-x}$  in the temperature range (100–300) K. For  $\text{UB}_{12-x}$ , the lattice thermal expansion is also presented.

**Table 4.** Linear fit of the lattice parameters and volumes with the temperature.

Compounds	$\text{UB}_{2-x}$			$\text{UB}_{4-x}$			$\text{UB}_{12-x}$	
Parameter	a	c	V	a	c	V	a	V
slope	$(1.0648 \pm 1.8127) \cdot 10^{-5}$	$(1.3111 \pm 0.2538) \cdot 10^{-4}$	$0.0043 \pm 0.0016$	$(7.3755 \pm 2.9109) \cdot 10^{-5}$	$(7.1264 \pm 3.0399) \cdot 10^{-5}$	$(8.83 \pm 3.64) \cdot 10^{-3}$	$(-2.3 \pm 1) \cdot 10^{-5}$	$-4.82 \pm 1.53) \cdot 10^{-3}$
intercept	$3.1172 \pm 0.0040$	$3.9641 \pm 0.0057$	$33.0589 \pm 0.2981$	$7.072 \pm 0.006$	$3.9662 \pm 0.0061$	$198.087 \pm 0.7423$	$7.4814 \pm 0.0021$	$419.0161 \pm 0.2836$
Adj-R <sup>2</sup>	0.5727	0.5067	0.2054	0.2942	0.2570	0.2725	0.2206	0.4076

### 3.2. Magnetic Susceptibility

The temperature dependencies of the magnetic susceptibilities ( $\chi$ ) for the three uranium borides are presented in Figure 3. For  $\text{UB}_{1.78}$ , the sample presents a temperature independent magnetic susceptibility—Pauli paramagnetism—with  $\chi_{\text{UB}1.78} \approx 0.55$  m emu/mol. A small anomaly is observed at approximately 50 K and is attributed to oxygen present in the SQUID magnetometer capsule. The field-dependence of the magnetization (inset of Figure 3a) is linear, and the curves measured at different temperatures have the same slope, as expected from a Pauli paramagnet. In previous work, Chachkhiani et al. [30] ( $\chi_{\text{UB}2-x} = 0.56$  m emu/mol) and Yamamoto et al. [7,8] ( $\chi_{\text{UB}2-x} = 0.55$  m emu/mol, Table 3 number 3) both described similar intrinsic Pauli magnetism on  $\text{UB}_2$  powders and single crystals, respectively. The second authors additionally described an increase in the susceptibility below 80 K ascribed to unknown magnetic impurities. This, together with other experimental results (e.g., De Haas–Van Alphen) and band calculations indicate that 5f electrons in  $\text{UB}_2$  have a very itinerant character. The close agreement of our data with  $\text{UB}_2$  single crystals shows that the physical properties are still retained in our bulk sample, despite the slightly lower boron content compared to  $\text{UB}_2$  ( $\text{UB}_{1.78}$ ). In addition, and contrary to Yamamoto et al., our sample does not present any visible magnetic impurity besides

the slight oxygen signal (coming from the equipment). Our results therefore confirm the temperature-independent character of the magnetic susceptibility of  $\text{UB}_2$  below 80 K and down to 2 K.

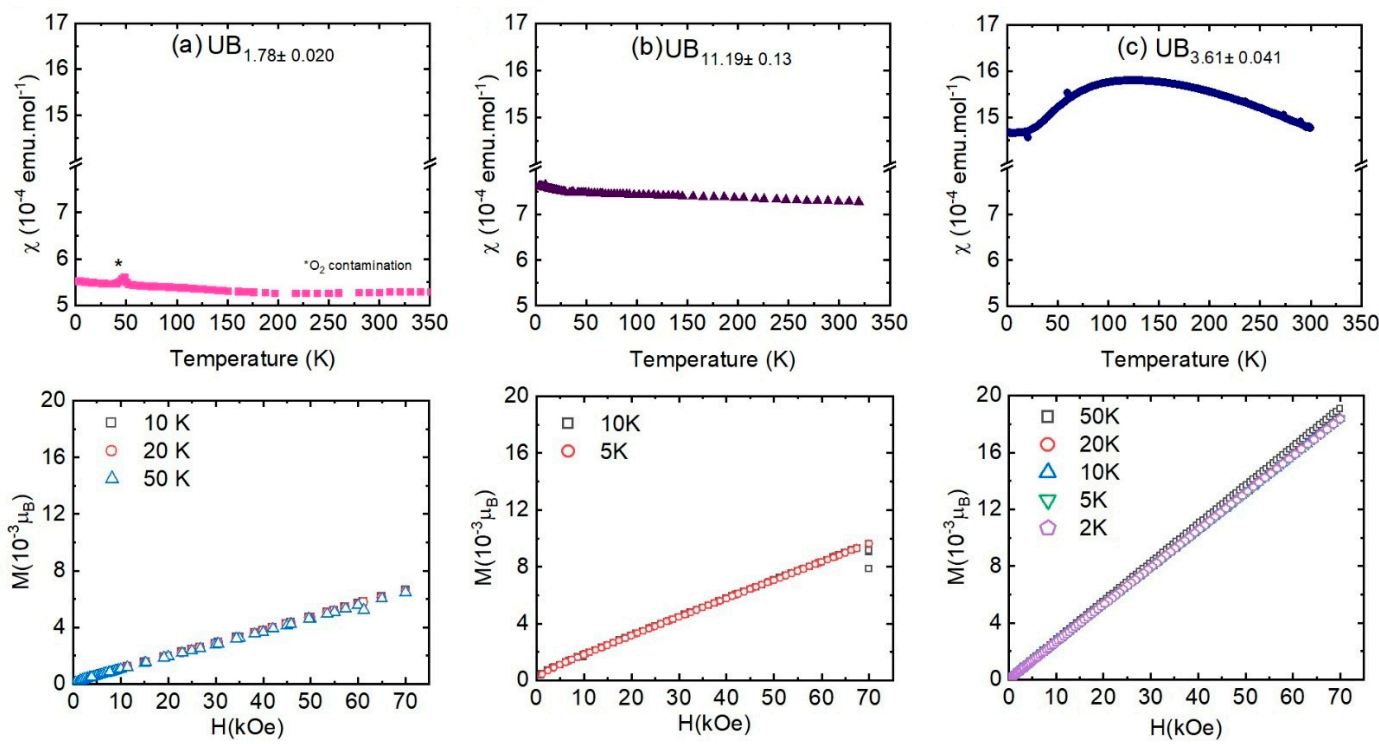


**Figure 3.** Magnetic susceptibility curves against temperature (top) and magnetization against field (bottom) for (a)  $\text{UB}_{1.78}$ , (b)  $\text{UB}_{11.19}$ , and (c)  $\text{UB}_{3.61}$ .

We find the magnetic susceptibility of  $\text{UB}_{11.19}$  to be nearly temperature independent, indicative of Pauli paramagnetism with  $\chi_{\text{UB}11.19} = 0.76$  memu/mol. The magnetization varies linearly versus applied magnetic field (inset of Figure 3b) and the curves at different temperatures superpose, as expected for a Pauli paramagnet. In the literature, Kasaya [31] and Tróć [32] reported  $\chi_{\text{UB}12-x} = 0.75$  memu/mol, similar to the present study. A second and more recent study performed jointly by Tróć et al. [10] and Samsel-Czekała et al. [11] reported a slightly smaller value with  $\chi_{\text{UB}12-x} \approx 0.65$  m emu/mol attributed to the presence of  $\text{UB}_4$  and paramagnetic impurities leading to a sharp increase at low temperature. Consistently, their magnetization vs. applied magnetic field curves are non-linear at 2 and 6 K and their slopes changes up to 14 K. We did not notice such behaviours (Figure 3b). Blum and Bertaut [21] published the smallest  $\text{UB}_{12-x}$  lattice parameter and reported a diamagnetic behaviour; this can be safely ruled out.

The magnetic susceptibility at room and low temperatures amounts to  $\chi_{\text{UB}3.61}^{\min} \sim 1.46$  memu/mol and displays a broad maximum ( $\chi_{\text{UB}3.61}^{\max} \sim 1.58$  memu/mol) in the temperature region 110–140 K. The magnetization varies linearly versus applied magnetic field (Figure 3c, lower), with a much larger slope than in  $\text{UB}_{1.78}$  and  $\text{UB}_{11.19}$ , consistent with the behaviour of their magnetic susceptibilities. The curves superpose from 2 to 20 K and the slope slightly changes at 50 K. From the magnetic susceptibilities published on  $\text{UB}_{4-x}$ , most authors have different results due to the range of non-stoichiometry (or impurities). Our results compare well with the magnetic susceptibility of Galatanu et al. [9] measured along the [100] direction of a single crystal, suggesting the possible occurrence of preferential orientation along the a-axis in our bulk sample. Their lattice parameters are similar to ours (Table 3, number 7). Additionally, our magnetization vs. magnetic field curve complements their data, as they recorded the curves for 2 K, 100 K, and higher temperatures. We can confirm the increase in linear slope at 50 K, which also occurs at

100 K. Our data also agree relatively well with those of Menovski et al. [19] on  $\text{UB}_{3.98}$  single crystals. They nonetheless reported a sharper maximum at 114 K with no magnetic ordering. The agreement between these previous studies and the present findings confirms the occurrence of the cross-over maximum and the robustness of this feature despite 5 wt%  $\text{UB}_{2-x}$  as a second phase. Overall,  $\text{UB}_{4-x}$  has delocalized electrons at low temperatures with a cross-over at approximately 110 K to localized 5f electrons at high temperatures [9] (Curie–Weiss law with an effective moment  $\mu_{\text{eff}} \approx 3.3 \mu_B/\text{U}$ ). In contrast, the polycrystalline sample measured by Wallash et al. [33] does not exhibit preferential orientation and no maximum, and Chachkhiani et al. [30] attributed the peak in the susceptibility in terms of antiferromagnetic ordering.

To sum up, we showed the influence of the boron content and additional boride phases on the magnetic susceptibilities.

### 3.3. Nuclear Magnetic Resonance

The NMR spectra recorded in static and magic angle spinning (MAS) (40 kHz) conditions, and their corresponding fits are presented in Figure 4.

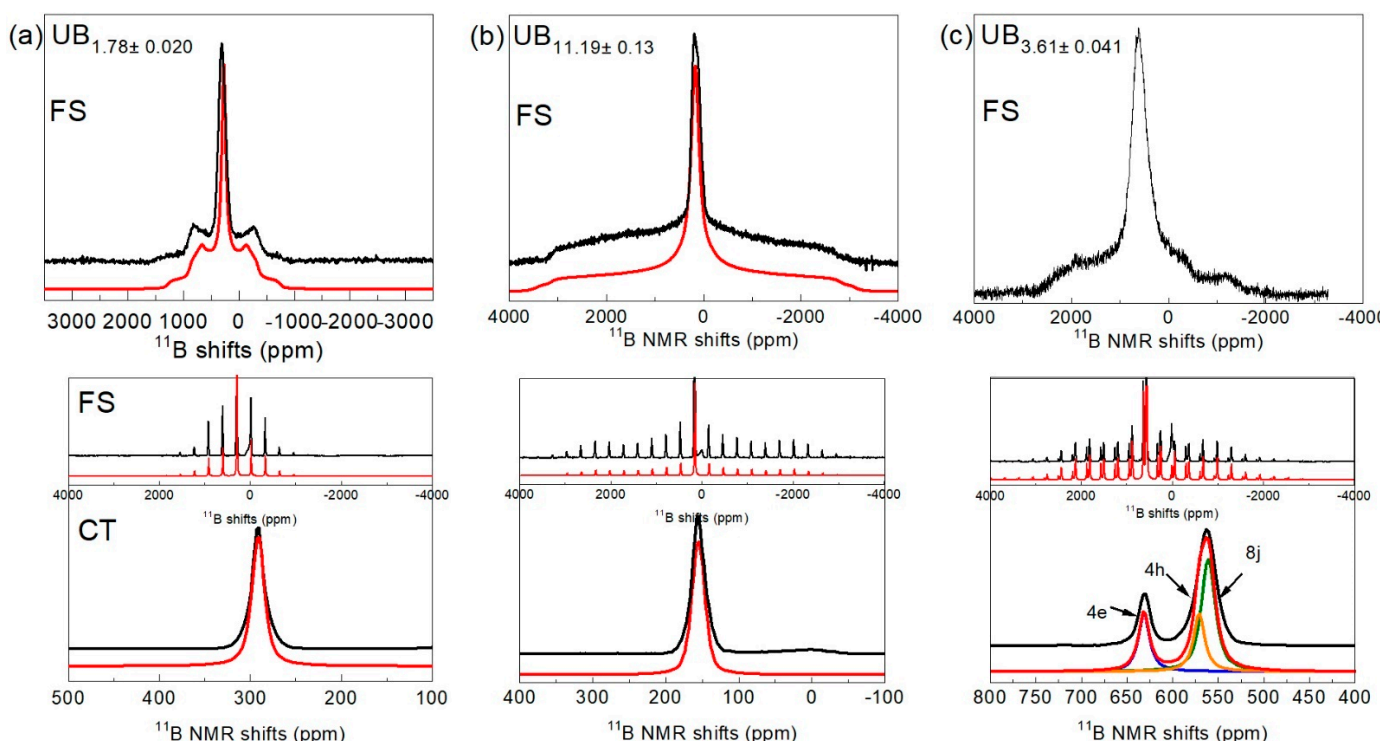


**Figure 4.**  $^{11}\text{B}$  static (upper) and MAS-NMR spectra (lower) for (a)  $\text{UB}_{1.78}$ , (b)  $\text{UB}_{11.19}$ , and (c)  $\text{UB}_{3.61}$  showing the central transition (CT) and the Full spectra (FS). The fits are the red lines.

The static  $^{11}\text{B}$  NMR spectra are defined by a typical powder pattern for a nuclear spin  $I = 3/2$  in the presence of first order quadrupolar interaction. The  $^{11}\text{B}$  MAS-NMR spectra are characterized by central peaks and their associated spinning sidebands due to the satellite transitions ( $\pm 3/2 \leftrightarrow \pm 1/2$ ). All the NMR parameters are given in Table 5. The shifts have, as expected, values largely above the common range expected for diamagnetic boron ( $\sim -3$  to  $\sim 20$  ppm) [34,35]. As expected from their crystal structure,  $\text{UB}_{1.78}$  and  $\text{UB}_{11.19}$  present one NMR peak in both static and MAS conditions. For  $\text{UB}_{3.61}$ , in addition to the peaks corresponding to the central transition, we could detect the signal of  $\text{UB}_{2-x}$  (3%), as shown by XRD. The crystal structure of  $\text{UB}_4$  possesses three different crystal B sites. The static NMR spectrum presents only one unresolved peak similar to the work published by Fukushima et al. [36]. By spinning the sample, the spectral resolution increases and we can identify two main peaks at 631.5 and  $\sim 563$  ppm. Nevertheless, the deconvolution

of the peak at 563 ppm was not possible using only one contribution due to a strong asymmetry. This peak was therefore fitted with two contributions at 571 and 561 ppm. Although the  $^{11}\text{B}$  peak at 561 ppm is clearly attributed to B3 (8j) due to its intensity being twice the one of the two other peaks, it is less straightforward for the B1 (4e) and B2 (4h) sites. To differentiate them, we proceeded as suggested by Creyghton et al. [37] and used the quadrupolar parameters. In fact, these authors stated that due to their similar crystal structures and the small c/a ratio [38,39] differences between  $\text{NdB}_4$  (0.568 [40]) and  $\text{LaB}_4$  (0.571 [41]), the quadrupolar parameters must follow the same sequence. In our case, the c/a ratio of  $\text{UB}_4$  (0.5624 [42]) is close enough to that of  $\text{YB}_4$  (0.5654 [43]) to apply the same principle. Therefore, as the peak at 631 ppm has the smallest  $C_Q$  it can be attributed to the B1 (4e) site similarly to  $\text{YB}_4$  [44], and the one at 571 ppm to B2 (4h). We want to further underline that for  $\text{NdB}_4$ , there is an inversion between B2 and B3 in the crystal structures reported in the literature. In fact, the P4/mbm structures B2 has the Wyckoff Symbol 4g and B3 8i.

**Table 5.**  $^{11}\text{B}$  NMR parameters Knight shifts ( $^{11}\text{B}K$ ), quadrupolar coupling constant ( $C_Q$ ), and asymmetry parameter ( $\eta_Q$ ) of the uranium borides compounds.

Compound Name		$^{11}\text{B}K$ (ppm)	FWHM (ppm)	$C_Q$ (kHz)	$\eta_Q$
$\text{UB}_{1.78}$	B1	303.6 <sup>a</sup> 291.6 <sup>b</sup>	— 16.8	298.4 <sup>a</sup>	0.2 <sup>a</sup>
	B1 (4e)	631.5	14.2	390 <sup>b</sup>	1 <sup>b</sup>
	B2 (4h)	571	14	560 <sup>b</sup>	0.9 <sup>b</sup>
	B3 (8j)	561.2	18	560 <sup>b</sup>	0.8 <sup>b</sup>
$\text{UB}_{11.19}$	B1	164.3 <sup>a</sup> 155.4 <sup>b</sup>	— 21.2	774.7 <sup>a</sup>	0.8 <sup>a</sup>
	AlB <sub>2</sub> [18]	$-10 \pm 5$		1.08	0
ZrB <sub>2</sub> [18]		−29		—	—
$\text{MgB}_2$ [45]		$40 \pm 10$		1.67	0
	4e	34.7		1.14	
	4h	12.6		1.46	
	8j	5.4		1.04	
$\text{YB}_4$ [44,46]	4e	42		0.69	0
	4h	47		1.1	0
	8j	18		0.8	0.5
	4e	$3300 (\pm 10\text{--}15\%)$		0.84	0
$\text{LaB}_4$ [37,47]	4h	$2300 (\pm 10\text{--}15\%)$		0.89	0.5
	8j	$2600 (\pm 10\text{--}15\%)$		1.244	0
$\text{ZrB}_{12}$ [18]		10		1.083	0.98
$\text{YB}_{12}$ [18]		25		1.08	0.93

The parameters were obtained <sup>a</sup> static and <sup>b</sup> 40 kHz.

We compared in Table 5 the NMR parameters of the  $\text{UB}_X$  with their isostructural  $\text{MB}_X$ :  $\text{UB}_{1.78}$  with the Pauli paramagnets AlB<sub>2</sub> and ZrB<sub>2</sub> [18] and the superconductor ( $T_c = 39$  K [46]) MgB<sub>2</sub> [48];  $\text{UB}_{3.61}$  with the diamagnetic YB<sub>4</sub> [44,46], the diamagnetic at room temperature [49] LaB<sub>4</sub> [37,47], and the antiferromagnetic (at 7 K) [49] NdB<sub>4</sub> [37,46]; finally,  $\text{UB}_{11.19}$  with the metallic ZrB<sub>12</sub> [18] and YB<sub>12</sub> [18,50]. All the  $\text{UB}_X$  possess higher shifts than their  $\text{MB}_X$  counterpart, most probably linked to the hybridization between the U5f and B2p orbitals. All the  $C_Q$  values in the  $\text{UB}_X$  are smaller compared to their  $\text{MB}_X$  counterparts, but they have similar asymmetry parameters.

To conclude the NMR observations, we found that despite the sample's lower boron content, only the expected number of  $^{11}\text{B}$  NMR peaks were detected. Due to the quadrupolar nucleus, the disorder might not be excluded as it can be expressed in the linewidth (Table 5). This result contrasts with the uranium carbides where additional  $^{13}\text{C}$  (spin 1/2) signals were detected as a fingerprint of the non-stoichiometry [51].

### 3.4. Infrared Spectroscopy

The FTIR spectra of the uranium borides are presented in Figure 5 and the main peaks positions are given in Table 6. According to the factor group analysis, the expected IR active modes for the idealized crystal structures at the Brillouin zone centre are ( $A_{2u} + E_{1u}$ ) for  $UB_2$ , ( $3A_{2u} + 9E_u$ ) for  $UB_4$ , and ( $3T_{1u}$ ) for  $UB_{12}$  [52]. All these optical phonons represent vibrations of the boron sublattice only.

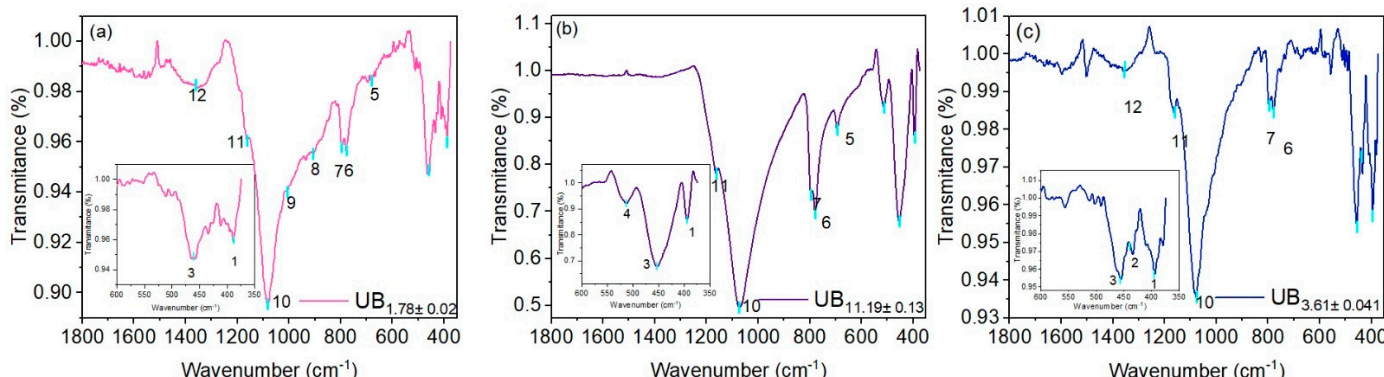


**Figure 5.** Infrared spectra of (a)  $UB_{1.78}$ , (b)  $UB_{11.19}$ , and (c)  $UB_{3.61}$ . The blue spots correspond to the main bands.

**Table 6.** Values of the main FTIR bands ( $\text{cm}^{-1}$ ). For  $UB_4$  extracted from the literature, dd corresponds to doubly degenerate mode. For  $ZrB_{12}$ , the numbers in bold are the active IR bands defined by the authors, with a star are the active IR bands defined by the Bilbao crystallographic database, and in italic are the active Raman bands. The frequencies presented for  $UB_{12}$  from ref. [52] correspond to Raman modes.

Present Study				Literature						
$UB_{1.78}$	$UB_{3.61}$	$UB_{11.19}$	$UB_4$ [53]	$ZrB_{12}$ [54]		$UB_{12}$ [54]	$UB_2$ [23]		$MgB_2$	
1	388	395	394	dd	315	$T_{1u}$	0	$E_{1u}$	393	$E_{1u}$ [55]
2	—	438			350	$T_{2u}$	198.3	$A_{2u}$	481	$A_{2u}$
3	463	456	453	dd	358	$T_{1u}$	206.6	$E_{2g}$	598	394/405 #
4	500	—	513		399	$T_{1g}$	478.1	$B_{1g}$	794	$E_{1u}$ [56]
5	680	—	693	dd	608	$E_u$	498.2			$A_{2u}$
6	778	778	778	dd	722	$A_{2g}$	518.8			401 #
7	796	796	795	dd	796	$E_g$	639.9	621	$E_{1u}$ [57]	320 #
8	907	—	—			$T_{2u}$	661.6		$A_{2u}$	390 #
9	1002	—	—			$T_{1g}$	693.6			
10	1083	1077	1073			$T_{1u}$	729.1			
11	1162	1162	1162			$T_{2g}$	801.7	748		
12	1360	1354	—			$T_{1u}$	854.2			
						$A_{2u}$	982.4			
						$E_g$	1010.1	971		
						$A_{1g}$	1078.3	1039		
						$T_{2g}$	1084.4	1088		

# calculated values for  $MgB_2$ .

To further analyze the data, we considered the calculated phonon spectra of  $UB_2$  and extracted the frequency of the optical modes (Table 6) [23]. Jossou et al. [23] calculated the doubly degenerate  $E_{1u}$  mode (B and U planes sliding along x, y) and the  $A_{2u}$  (B and U planes moving against each other) modes at  $393$  and  $481\text{ cm}^{-1}$ , respectively. These results are similar to the values obtained for the modes at  $388\text{ cm}^{-1}$  and  $465\text{ cm}^{-1}$ . The difference might be due to different lattice parameters (Table 3 number 4) and characteristics of the different stoichiometries. The additional peaks can be attributed to a loss of the local

symmetry and the Raman forbidden modes can be relaxed, which indicates a reduction of symmetry [58]. The high frequency modes manifested as broad intense bands centred at  $1002\text{ cm}^{-1}$ ,  $1162\text{ cm}^{-1}$ , and  $1360\text{ cm}^{-1}$  might be a combination of multiple modes located near the  $463\text{ cm}^{-1}$  mode [58,59]. It is worth comparing  $\text{UB}_{1.78}$  with  $\text{MgB}_2$  as, due to its superconductivity [48], its optical properties have been extensively studied. The values of the IR active phonon modes in  $\text{UB}_2$  are relatively similar to the one reported experimentally [58,59] and theoretically [55–57] for  $\text{MgB}_2$  (Table 6).

We compared  $\text{UB}_{12}$  with the modes previously calculated for  $\text{ZrB}_{12}$  [54] (Table 6), as they should qualitatively give similar FTIR spectra. We believe that the correct IR active modes are the  $3T_{1u}$ . The first  $T_{1u}$  mode at  $206.6\text{ cm}^{-1}$  is not visible in our IR spectrum, but the two other  $T_{1u}$  modes, at  $729.1\text{ cm}^{-1}$  and  $854.2\text{ cm}^{-1}$ , might correspond to the modes at  $778\text{ cm}^{-1}$  and  $795\text{ cm}^{-1}$  (Table 6). Similar to the FTIR from the  $\text{MB}_{12}$  series [54], silent modes appear on our spectrum as the local distortions can break the local symmetry, and the selection rules are then lifted. This peculiar behaviour seems typical for metal borides. Thus, the modes at  $1073\text{ cm}^{-1}$  and  $1162\text{ cm}^{-1}$  can be attributed to the Raman forbidden modes  $E_g/A_{1g}$  and  $T_{2g}$ , respectively. It must be noted that based on the present data, an unambiguous attribution is not possible.

To our knowledge, Lopez-Bezanilla [53] calculated the only phonon spectra on  $\text{UB}_4$ . The author reported 12 out of the 31 optical modes and did not discuss their nature. A recent work by Surucu et al. [60] on  $\text{LaB}_4$  reported all the optical modes and determined a phonon range of  $264\text{--}1072\text{ cm}^{-1}$ , which therefore implies that a larger range will be expected for  $\text{UB}_4$ . For this compound, we therefore cannot go much further in the spectral analysis but noted that the observed optical modes in the IR spectrum represent the whole frequency range of the calculated phonon spectrum ( $315\text{--}796\text{ cm}^{-1}$ ) (Table 6). The mode at  $1007\text{ cm}^{-1}$  has a similar value as the forbidden Raman mode  $B_{1g}$  predicted for  $V = 199\text{ \AA}$  at  $\sim 1000\text{ cm}^{-1}$  (see ref. [61]). Finally, it is worth noting that the characteristic bands observed for  $\text{UB}_{2-x}$  ( $388\text{ cm}^{-1}$  and  $465\text{ cm}^{-1}$ ) are also detected on the  $\text{UB}_{4-x}$  spectrum, in agreement with the XRD and NMR results.

From this FTIR study and the detection of additional modes, we can observe the expected structural defects that are lifting the selection rules stated from the idealized structure.

#### 4. Conclusions

In the present study, we revisited the binary system U-B via its three samples with nominal composition  $\text{UB}_2$ ,  $\text{UB}_4$ , and  $\text{UB}_{12}$ . Within the uncertainty of the chemical and oxygen content analyses, purity of the samples and their U/B ratio were well characterised. The data supported the view proposed by Brewer et al. about their range of non-stoichiometry described in the literature. The composition definition of each sample is essential to link the properties and likely to explain the difference observed in literature with the lattice parameters. The X-ray diffraction patterns show the purity of the samples for  $\text{UB}_{12-x}$  and  $\text{UB}_{2-x}$ , whereas a minor content of  $\text{UB}_{2-x}$  could be found for  $\text{UB}_{4-x}$ . Furthermore, their high intensity peaks show long range order on the arc melted as cast samples. In the low range of temperature  $100\text{ K}\text{--}300\text{ K}$ , XRD did not indicate a clear negative thermal expansion in  $\text{UB}_{12-x}$  as its counterpart  $\text{LuB}_{12}$ . Although influenced by the boron content, the magnetic properties agree to a certain extent with the literature data. The NMR analyses show the influence of the hybridisation between  $\text{U}5f$  and  $\text{B}2p$ . The FTIR spectra confirm the local composition effects and the disorder. We believe that our study will trigger the curiosity of theoreticians to draw models with clear references.

**Supplementary Materials:** The following supporting information can be downloaded at: <https://www.mdpi.com/article/10.3390/min12010029/s1>, Figure S1: Full X-ray diffraction patterns and corresponding fits for the uranium borides.

**Author Contributions:** R.E. and P.A.C. synthesized the samples. R.E. and L.M. characterized and analyzed the XRD. J.-C.G., E.C. and L.M. performed and analyzed the magnetic analyses. R.E., L.M. and M.N. performed and analyzed the FTIR data. T.C., C.S. and L.M. performed and analyzed the

NMR experiments. All authors contributed equally to writing the paper. All authors have read and agreed to the published version of the manuscript.

**Funding:** JRC-ITU (06-09/2013).

**Acknowledgments:** The authors thank Sven Pfirmann for his support with the NMR, Olaf Walter for his advice concerning the single crystal XRD, and Joseph Somers for fruitful discussions.

**Conflicts of Interest:** The authors declare no conflict of interest.

## References

1. Lupinetti, A.J.; Fife, J.L.; Garcia, E.; Dorhout, P.K.; Abney, K.D. Low-temperature synthesis of uranium tetraboride by solid-state metathesis reactions. *Inorg. Chem.* **2002**, *41*, 2316–2318. [[CrossRef](#)]
2. Gossé, S.; Alpettaz, T.; Géneau, C.; Allegri, P. High temperature thermochemistry of (U-Pu)O<sub>2</sub> MOX fuel with B<sub>4</sub>C absorber—Application to severe accidents in SFR. In Proceedings of the International Conference on Fast Reactors and Related Fuel Cycles: Safe Technologies and Sustainable Scenarios, Paris, France, 4–7 March 2013.
3. Kardoulaki, E.; White, J.T.; Byler, D.D.; Frazer, D.M.; Shivprasad, A.P.; Saleh, T.A.; Gong, B.; Yao, T.; Lian, J.; McClellan, K.J. Thermophysical and mechanical property assessment of UB<sub>2</sub> and UB<sub>4</sub> sintered via spark plasma sintering. *J. Alloys Compd.* **2020**, *818*, 153216. [[CrossRef](#)]
4. Howlett, B.W. A Note on the Uranium-Boron Alloy System. *J. Inst. Met.* **1959**, *88*, 91–92.
5. Chevalier, P.Y.; Fischer, E. Thermodynamic modelling of the C-U and B-U binary systems. *J. Nucl. Mater.* **2001**, *288*, 100–129. [[CrossRef](#)]
6. Brewer, L.; Sawyer, D.L.; Templeton, D.H.; Dauben, C.H. A study of the refractory borides. *J. Am. Ceram. Soc.* **1951**, *34*, 173–179. [[CrossRef](#)]
7. Yamamoto, E.; Honma, T.; Haga, Y.; Inada, Y.; Aoki, D.; Suzuki, N.; Settai, R.; Sugawara, H.; Sato, H.; Yoshichika, Ō. Electrical and thermal properties of UB<sub>2</sub>. *J. Phys. Soc. Jpn.* **1999**, *68*, 972. [[CrossRef](#)]
8. Yamamoto, E.; Honma, T.; Haga, Y.; Inada, Y.; Aoki, D.; Tokiwa, Y.; Suzuki, N.; Miyake, K.; Yoshichika, Ō. Magnetoresistance and de Haas Van Alphen effect in UB<sub>2</sub>. *J. Phys. Soc. Jpn.* **1999**, *68*, 3347–3351. [[CrossRef](#)]
9. Galatanu, A.; Yamamoto, E.; Hagab, Y.; Onuki, Y. Magnetic behaviour of UB<sub>4</sub> at high temperatures. *Phys. B Condens. Matter.* **2006**, *378*, 999–1000. [[CrossRef](#)]
10. Troć, R.; Wawryk, R.; Pikul, A.; Shitsevalova, N. Physical properties of cage-like compound UB<sub>12</sub>. *Philos. Mag.* **2015**, *95*, 2343–2363. [[CrossRef](#)]
11. Samsel-Czekała, M.; Talik, E.; Tróć, R.; Shitsevalova, N. Electronic structure of cage-like compound UB<sub>12</sub>—Theory and XPS experiment. *J. Alloys Compd.* **2014**, *615*, 446–450. [[CrossRef](#)]
12. Chipaux, R. Contribution à l'étude de la cristallochimie et des propriétés électroniques des borures d'actinides. Ph.D. Thesis, Université d'Aix-Marseille II, Marseille, France, 1988.
13. Massiot, D.; Farnan, I.; Gautier, N.; Trumeau, D.; Trokiner, A.; Coutures, J.P. <sup>71</sup>Ga and <sup>69</sup>Ga nuclear magnetic resonance study of β-Ga<sub>2</sub>O<sub>3</sub>: Resolution of four—and six-fold coordinated Ga sites in static conditions. *Solid State Nucl. Magn. Reson.* **1995**, *4*, 241–248. [[CrossRef](#)]
14. Martel, L.; Griveau, J.-C.; Eloirdi, R.; Selfslag, C.; Colineau, E.; Caciuffo, R. Ferromagnetic ordering in NpAl<sub>2</sub>: Magnetic susceptibility and <sup>27</sup>Al nuclear magnetic resonance. *J. Magn. Magn. Mater.* **2015**, *387*, 72–76. [[CrossRef](#)]
15. Massiot, D.; Fayon, F.; Capron, M.; King, I.; Le Calvé, S.; Alonso, B.; Durand, J.O.; Bujoli, B.; Gan, Z.; Hoatson, G. Modelling one—and two-dimensional solid-state NMR spectra. *Magn. Reson. Chem.* **2002**, *40*, 70–76. [[CrossRef](#)]
16. Angeli, F.; Charpentier, T.; De Ligny, D.; Cailleteau, C. Boron speciation in soda-lime borosilicate glasses containing zirconium. *J. Am. Ceram. Soc.* **2010**, *93*, 2693–2704. [[CrossRef](#)]
17. Flotow, H.E.; Osborne, D.W.; O'Hare, P.A.G.; Settle, J.L.; Mrazek, F.C.; Hubbard, W.N. Uranium Diboride: Preparation, Enthalpy of Formation at 298.15°K, Heat Capacity from 1° to 350°K, and Some Derived Thermodynamic Properties. *J. Chem. Phys.* **1969**, *51*, 583–592. [[CrossRef](#)]
18. Akopov, G.; Mak, W.H.; Koumoulis, D.; Yin, H.; Owens-Baird, B.; Yeung, M.T.; Muni, M.H.; Lee, S.; Roh, I.; Sobell, Z.C.; et al. Synthesis and characterization of single-phase metal dodecaboride solid solutions: Zr<sub>1-x</sub>Y<sub>x</sub>B<sub>12</sub> and Zr<sub>1-x</sub>U<sub>x</sub>B<sub>12</sub>. *J. Am. Chem. Soc.* **2019**, *141*, 9047–9062. [[CrossRef](#)]
19. Menovsky, A.; Franse, J.J.M.; Klaasse, J.C.P. The crystal growth of uranium tetraboride UB<sub>4</sub> from the melt. *J. Cryst. Growth* **1984**, *70*, 519–522. [[CrossRef](#)]
20. Dancausse, J.-P.; Gering, E.; Heathman, S.; Benedict, U.; Gerward, L.; Staun Olsen, S.; Hulliger, F. Compression study of uranium borides UB<sub>2</sub>, UB<sub>4</sub> and UB<sub>12</sub> by synchrotron X-ray diffraction. *J. Alloys Compd.* **1992**, *189*, 205–208. [[CrossRef](#)]
21. Blum, P.; Bertaux, F. Contribution à l'étude des borures à teneur élevée en bore. *Acta Cryst.* **1954**, *7*, 81–86. [[CrossRef](#)]
22. Matkovich, V.I.; Economy, J.; Giese jr., R.F. Barrett, R. The structure of metallic dodecaborides. *Acta Cryst.* **1965**, *19*, 1056–1058. [[CrossRef](#)]
23. Jossou, E.; Oladimeji, D.; Malakkal, L.; Middleburgh, S.; Szpunar, B.; Szpunar, J. First-principles study of defects and fission product behavior in uranium diboride. *J. Nucl. Mater.* **2017**, *494*, 147–156. [[CrossRef](#)]

24. Chipaux, R.; Cecilia, G.; Beauvy, M.; Tróć, R. Capacité thermique à haute température de UBe<sub>13</sub>, ThBe<sub>13</sub> et UB<sub>4</sub>. *J. Less Common Met.* **1986**, *121*, 347–351. [[CrossRef](#)]
25. Turner, J.; Martini, F.; Buckley, J.; Phillips, G.; Middleburgh, S.C.; Abram, T.J. Synthesis of candidate advanced technology fuel: Uranium diboride (UB<sub>2</sub>) via carbo/borothermic reduction of UO<sub>2</sub>. *J. Nucl. Mater.* **2020**, *540*, 152388. [[CrossRef](#)]
26. Guo, H.; Wang, J.; Chen, D.; Tian, W.; Cao, S.; Chen, D.; Tan, C.; Deng, Q.; Qin, Z. Boro/carbothermal reduction synthesis of uranium tetraboride and its oxidation behavior in dry air. *J. Am. Ceram. Soc.* **2019**, *102*, 1049–1056. [[CrossRef](#)]
27. Evitts, L.J.; Middleburgh, S.C.; Kardoulaki, E.; Ipatova, I.; Rushton, M.J.D.; Lee, W.E. Influence of boron isotope ratio on the thermal conductivity of uranium diboride (UB<sub>2</sub>) and zirconium diboride (ZrB<sub>2</sub>). *J. Nucl. Mater.* **2020**, *528*, 151892. [[CrossRef](#)]
28. Okada, Y.; Tokumaru, Y. Precise determination of lattice parameter and thermal expansion coefficient of silicon between 300 and 1500 K. *J. Appl. Phys.* **1984**, *56*, 314–320. [[CrossRef](#)]
29. Czopnik, A.; Shitsevalova, N.; Pluzhnikov, V.; Krivchikov, A.; Paderno, Y.; Onuki, Y. Low-temperature thermal properties of yttrium and lutetium dodecaborides. *J. Phys. Condens. Matter.* **2005**, *17*, 5971–5985. [[CrossRef](#)]
30. Chachkhiani, Z.B.; Chachkhiani, L.G.; Chechernikov, V.I.; Slovyanikh, V.K. Magnetic properties of thorium and uranium borides and U<sub>1-x</sub>Th<sub>x</sub>B<sub>4</sub> solid solutions. *Sov. Phys. J.* **1982**, *25*, 621–623. [[CrossRef](#)]
31. Kasaya, M.; Iga, F.; Katoh, K.; Takegahara, K.; Kasuya, T. Magnetic and transport properties of uranium borides, UB<sub>12</sub>, Ulr<sub>3</sub>B<sub>2</sub> and UOs<sub>3</sub>B<sub>2</sub>. *J. Magn. Magn. Mater.* **1990**, *90*, 521–522. [[CrossRef](#)]
32. Troć, R.; Trzebiatowski, W.; Piprek, K. Magnetic properties of uranium borides and of uranium beryllide UBe<sub>13</sub>. *Bull. Acad. Polon. Sci. Ser. Sci. Chim.* **1971**, *19*, 427.
33. Wallash, A.; Crow, J.; Fisk, Z. Susceptibility, magnetization, and specific heat in the paramagnetic and ferromagnetic regions of (Y<sub>1-x</sub>U<sub>x</sub>)B<sub>4</sub>. *J. Appl. Phys.* **1985**, *57*, 3143–3145. [[CrossRef](#)]
34. Mackenzie, K.J.D.; Smith, M.E. *M multinuclear Solid-State NMR of Inorganic Materials*; Cahn, R., Ed.; Elsevier: Amsterdam, The Netherlands, 2002.
35. Angel Wong, Y.-T.; Bryce, D.L. Recent Advances in <sup>11</sup>B Solid-State Nuclear Magnetic Resonance Spectroscopy of Crystalline Solids. *Annu. Rep. NMR Spectrosc.* **2018**, *93*, 213–279.
36. Fukushima, E.; Strubeing, V.O.; Hill, H.H. Induced Paramagnetism in Uranium Alloys: A Boron NMR Study of Alloys Formed between UB<sub>4</sub> and YB<sub>4</sub>. *J. Phys. Soc. Jpn.* **1975**, *39*, 921–926. [[CrossRef](#)]
37. Creighton, J.H.N.; Locher, P.R.; Buschow, K.H.J. Nuclear magnetic resonance of <sup>11</sup>B at the three boron sites in rare-earth tetraborides. *Phys. Rev. B* **1973**, *7*, 4829–4843. [[CrossRef](#)]
38. *Crystal Structures*, 2nd ed.; Interscience: New York, NY, USA, 1964; Volume 2.
39. Fisk, Z.; Cooper, A.S.; Schmidt, P.H.; Castellano, R.N. Preparation and lattice parameters of the rare earth tetraborides. *Mater. Res. Bull.* **1972**, *7*, 285–288. [[CrossRef](#)]
40. Roger, J.; Babizhetskyy, V.; Jardin, R.; Halet, J.-F.; Guérin, R. Solid state phase equilibria in the ternary Nd–Si–B system at 1270 K. *J. Alloys Compd.* **2006**, *415*, 73–84. [[CrossRef](#)]
41. Kato, K.; Kawada, I.; Oshima, C.; Kawai, S. Lanthanum tetraboride. *Acta Cryst. B* **1974**, *B30*, 2933–2934. [[CrossRef](#)]
42. Zalkin, A.; Templeton, D.H. The crystal structures of CeB<sub>4</sub> ThB<sub>4</sub> and UB<sub>4</sub>. *Acta Cryst.* **1953**, *6*, 269–272. [[CrossRef](#)]
43. Giese, R.F., Jr.; Matkovich, V.I.; Economy, J. The crystal structure of YB<sub>4</sub>. *Z. Krist.* **1965**, *122*, 423–432. [[CrossRef](#)]
44. Jäger, B.; Paluch, S.; Wolf, W.; Herzig, P.; Źogał, O.J.; Shitsevalova, N.; Paderno, Y. Characterization of the electronic properties of YB<sub>4</sub> and YB<sub>6</sub> using <sup>11</sup>B NMR and first-principles calculations. *J. Alloys Compd.* **2004**, *383*, 232–238. [[CrossRef](#)]
45. Baek, S.H.; Suh, B.J.; Pavarini, E.; Borsa, F.; Barnes, R.G.; Bud'ko, S.L.; Canfield, P.C. NMR spectroscopy of the normal and superconducting states of MgB<sub>2</sub> and comparison to AlB<sub>2</sub>. *Phys. Rev. B* **2002**, *66*, 104510. [[CrossRef](#)]
46. Źogał, O.J.; Florian, P.; Massiot, D.; Paluch, S.; Shitsevalova, N.; Borshchevsky, D.F. <sup>11</sup>B and <sup>89</sup>Y MAS NMR and magnetic characterization of YB<sub>4</sub>. *Solid State Commun.* **2009**, *149*, 693–696. [[CrossRef](#)]
47. Schmitt, R.; Blaschkowski, B.; Eichele, K.; Meyer, H.-J. Calcium Tetraboride Does It Exist? Synthesis and Properties of a Carbon-Doped Calcium Tetraboride That Is Isotypic with the Known Rare Earth Tetraborides. *Inorg. Chem.* **2006**, *45*, 3067–3073.
48. Nagamatsu, J.; Nakagawa, N.; Muranaka, T.; Zenitani, Y.; Akimitsu, J. Superconductivity at 39 K in magnesium diboride. *Nature* **2001**, *410*, 63–64. [[CrossRef](#)]
49. Buschow, K.H.J.; Creighton, J.H.N. Magnetic Properties of Rare Earth Tetraborides. *J. Chem. Phys.* **1972**, *57*, 3910–3914. [[CrossRef](#)]
50. Fojud, Z.; Herzig, P.; Źogał, O.J.; Pietraszko, A.; Dukhnenko, A.; Jurga, S.; Shitsevalova, N. Electric-field-gradient tensor and boron site-resolved <sup>11</sup>B NMR in single-crystalline YB<sub>12</sub>. *Phys. Rev. B* **2007**, *75*, 184102. [[CrossRef](#)]
51. Carvajal Nuñez, U.; Martel, L.; Prieur, D.; Lopez Honorato, E.; Eloirdi, R.; Farnan, I.; Vitova, T.; Somers, J. Coupling XRD, EXAFS, and <sup>13</sup>C NMR to study the effect of the carbon stoichiometry on the local structure of UC<sub>1±x</sub>. *Inorg. Chem.* **2013**, *19*, 11669–11676. [[CrossRef](#)]
52. Kroumova, E.; Aroyo, M.I.; Perez Mato, J.M.; Kirov, A.; Capillas, C.; Ivantchev, S.; Wondratschek, H. Bilbao Crystallographic Server: Useful databases and tools for phase transitions studies. In *Phase Transitions 76*; Nos. 1–2; 2003; pp. 155–170. [[CrossRef](#)]
53. Lopez-Bezanilla, A. f-Orbital based Dirac states in a two-dimensional uranium compound. *J. Phys. Mater.* **2020**, *3*, 024002. [[CrossRef](#)]
54. Werheit, H.; Filipov, V.; Shirai, K.; Dekura, H.; Shitsevalova, N.; Schwarz, U.; Armbrüster, M. Raman scattering and isotopic phonon effects in dodecaborides. *J. Phys. Condens. Matter* **2011**, *23*, 065403. [[CrossRef](#)]

55. Bohnen, K.-P.; Heid, R.; Renker, B. Phonon Dispersion and Electron-Phonon Coupling in MgB<sub>2</sub> and AlB<sub>2</sub>. *Phys. Rev. Lett.* **2001**, *86*, 5771–5774. [[CrossRef](#)]
56. Kong, Y.; Dolgov, O.V.; Jepsen, O.; Andersen, O.K. Electron-phonon interaction in the normal and superconducting states of MgB<sub>2</sub>. *Phys. Rev. B* **2001**, *64*, 020501. [[CrossRef](#)]
57. Kortus, J.; Mazin, I.I.; Belashchenko, K.D.; Antropov, V.P.; Boyer, L.L. Superconductivity of metallic boron in MgB<sub>2</sub>. *Phys. Rev. Lett.* **2001**, *86*, 4656–4659. [[CrossRef](#)] [[PubMed](#)]
58. Alarco, J.A.; Chou, A.; Talbot, P.C.; Mackinnon, I.D.R. Phonon Modes of MgB<sub>2</sub>: Super-lattice Structures and Spectral Response. *Phys. Chem. Chem. Phys.* **2014**, *16*, 24443–24456. [[CrossRef](#)] [[PubMed](#)]
59. Sundar, C.S.; Bharathi, A.; Premila, M.; Kalavathi, S.; Reddy, G.L.N.; Sastry, V.S.; Hariharan, Y.; Radhakrishnan, T.S. Infrared absorption in superconducting MgB<sub>2</sub>. *arXiv* **2001**, arXiv:0104354.
60. Surucu, G.; Ozışık, H.; Deligoz, E.; Shein, I.R.; Matovnikov, A.V.; Mitroshenkov, N.V.; Morozov, A.V.; Novikov, V.V. Electronic and thermodynamic properties of lanthanum tetraboride on low-temperature experimental and ab-initio calculation data. *J. Alloys Compd.* **2020**, *862*, 158020. [[CrossRef](#)]
61. Werheit, H.; Filipov, V.; Shitsevalova, N.; Armbrüster, M.; Schwarz, U.; Ievdokimova, A.; Muratov, V.; Gurin, V.N.; Korsukova, M.M. Raman scattering in rare earths tetraborides. *Solid State Sci.* **2014**, *31*, 24–32. [[CrossRef](#)]